CORA Cork Open Research Archive
Cartlann Taighde Oscailte Chorcaí

Title	Polaron assisted hopping mechanism in microwave processed Nd doped second layered aurivillius SrBi2Nb2O9 ceramics
Authors	Pritam, Anurag
Publication date	2024-10-17
Original Citation	Pritam, A. (2024) 'Polaron assisted hopping mechanism in microwave processed Nd doped second layered aurivillius SrBi2Nb2O9 ceramics', Ceramics International, 50(22), pp.48343-48353. https://doi.org/10.1016/j.ceramint.2024.09.184
Type of publication	Article (peer-reviewed)
Link to publisher's version	10.1016/j.ceramint.2024.09.184
Rights	© 2024, Elsevier Ltd and Techna Group S.r.l. All rights are reserved, including those for text and data mining, AI training, and similar technologies. This manuscript version is made available under the CC BY-NC-ND 4.0 license. - https://creativecommons.org/licenses/by-nc-nd/4.0/
Download date	2026-11-02 03:31:29
Item downloaded from	https://hdl.handle.net/10468/16645

UCC
University College Cork, Ireland
Coláiste na hOllscoile Corcaigh

Polaron Assisted Hopping Mechanism in Microwave Processed Nd doped Second Layered Aurivillius $SrBi_2Nb_2O_9$ Ceramics.

Anurag Pritam [1,2*]

[1] *Tyndall National Institute, University College Cork, Cork, Ireland*

[2] *Department of Physics, School of Natural Sciences, Shiv Nadar Institution of Eminence, Greater Noida, India.*

Address of correspondence:

Email: anurag.pritam64@gmail.com

Keywords: Rietveld refinement, Maxwell-Wagner distribution, Cole-Cole Plot, polaron hopping, activation energy, modulus spectroscopy.

Abstract

The polycrystalline $Sr_{0.8}Sn_{0.2}Bi_{1.75}Nd_{0.25}Nb_2O_9$ (NdSBN) was synthesized using the green synthesis microwave sintering method, which significantly reduced the processing parameters of the NdSBN ceramics**. Orthorhombic crystal structure with $A2_1am$ symmetry was revealed by Rietveld refinement study**, **whereas the doping-induced strain and crystallite size was studied using Williamson Hall method**. Crossectional SEM micrographs confirm the plate-like structure, with an average grain size of 273.7 nm. A **diffuse type of phase transition was observed at 345 ^oC, which usually arises due to compositional fluctuations and mobile oxygen vacancies;** further, the diffusiveness of the NdSBN was studied using Uchino and Nomura function, a modified version of Curie-Weiss law (CW). The frequency and temperature-dependent dielectric study of NdSBN ceramics display a Maxwell-Wagner relaxation with a high loss in a low frequency regime, possibly due to the presence of leakage current in the solid solution. **Frequency dependent AC conductivity obeys Jonscher's power law, whereas DC conductivity supports polaron assisted hopping in NdSBN composition with dual activation energies of 0.55 eV and 0.75 eV, which correspond to electrons and ions, respectively**. The non-Debye type relaxation mechanism in conjunction with negative temperature coefficient of resistance (NTCR) behavior was demonstrated by temperature dependent impedance spectroscopy, while modulus spectroscopy confirmed the multiple relaxation processes in NdSBN ceramics.

Introduction

Due to extensive intrusion of electronic devices in our daily lives as manifested by portable electronics to smart devices has sparked a prerequisite for the design and development of environment-friendly electronic components. For the last couple of decades, researchers have huffed and puffed with the concept of fabricating electronic devices/components with advanced features like high mechanical adaptability, lightweight, sustainability, improved electrical properties, and eco-friendliness. This venture can be achieved by appropriate permutations and combinations of functional materials[1–3]. Ceramics have always been in demand for numerous applications including memory devices, mechanical sensors, electrodes, catalysts, energy storage devices, high-temperature applications, and many more. However, the comprehensive usage of lead-based ceramics and their derivatives has seen exponential growth in recent times as lead-based derivates are easily available in nature and display high remnant polarization. However, the long term utilization of lead poses a significant threat to human health, and ecology due to its toxicity, thus compelling researchers across the globe to search for an alternative of Lead-based composition with similar properties. In order to achieve high-performance lead-free materials, it is essential to determine the bottleneck and crucial parameters, which need to be tailored for enhanced performance [4–8]. Out of various structured families, the Aurivillius layered material i.e. Bismuth layered structured ferroelectrics (BLSFs) outperformed lead-based ferroelectrics due to its superior fatigue characteristics, high Curie temperature, remarkable ferroelectric, pyroelectric, and piezoelectric properties, which make them eligible candidates to be used for several industrial applications. This class of material was first discovered by B. Aurivillius in 1949 having the chemical formula $(Bi_2O_2)^{2+}(A_{m-1}B_mO_{3m+1})^{2-}$ where A-site is taken by mono, dia, and trivalent ion (K^+, Ca^{2+}, Ba^{2+}, Bi^{3+}, etc.), B-site is occupied by transitional elements like (Ti^{4+}, Nb^{5+}, Ta^{4+}, Mo^{6+}, etc.) and m is an integer which denotes the number of BO_6 octahedral sandwiched in between the $(Bi_2O_2)^{2+}$ layers. Among various BSLFs, the $SrBi_2Nb_2O_9$ (SBN) belongs to the n=2 group having disordered uniaxial ferroelectric properties. SBN and its solid solution have gained significant attention due to its exceptional control over rattling space on the ferroelectric and piezoelectric properties[9–13]. On the other hand, substantial dielectric loss along with low residual polarization present some challenges for the SBN. The most effective approach to address these issues and improve its electrical properties is by appropriate cation substitution. SBN offers an advantageous crystal structure, flexible A and B site occupancy, and a high degree of compositional flexibility to customize the necessary features. There are reports which suggest that the substitution on A site in SBN enhances the rotation of NbO_6 octahedra in the a-b plane which significantly improves the dielectric and electrical properties of the SBN and its solid solution. **Literature suggests that polarization of SBN can be further enhanced by doping the parent composition with rare earth (RE) substitutions such as Ce^{3+}, Nd^{3+}, La^{3+}, Pr^{3+}, Gd^{3+}, and Y^{3+}as RE elements substantially reduce the generation of oxygen vacancies in the system due to their peculiar electronic structure and lattice distortion**[1, 14–18]. Another factor that strongly influences the properties and performance of BSLFs is their processing technique, SBN can be synthesized using numerous techniques, such as hot pressing, reactive sintering, double-stage sintering, conventional sintering, and microwave sintering. Conventional sintering is the most common and widely used technique to synthesize

SBN ceramics, which utilizes lots of time and energy, since it involves two steps of heating, in the form of calcination and sintering. Conversely, microwave heating is a rapid sintering technique that works on the direct conversion of electromagnetic energy into thermal energy. Additionally, it possesses several advantages over alternative methods, including rapid heating, less product damage, uniform heating, reduced greenhouse gas emissions, and many more [19–21].

Consequently, from the meticulous investigation of the reported literature on second layered Aurivillius material, it has been understood that minimal reports are available on multiple sites doping and its influence on electrical properties in SBN. **The available electric and dielectric studies in SBN have been rarely found to incorporate the aspects of the non-Debye type conduction mechanism, multiple relaxation processes, large polaron hopping, etc. Therefore, the present work demonstrates the detailed investigation of structural contribution to the electrical transport mechanism and dielectric relaxation process in $Sr_{0.8}Sn_{0.2}Bi_{1.75}Nd_{0.25}Nb_2O_9$ (NdSBN) ceramics** prepared through novel microwave sintering technique. Numerous dielectric-derived immittance functions like Z*, M*, and σ* have been investigated in order to gain a comprehensive understanding of the electrical properties of the NdSBN ceramics over a wide range of temperatures (50-550 ^oC) and frequencies (20 Hz -2 MHz).

2. Experimental Details

2.1 Materials and Methods

The stoichiometric ratios of Bi_2O_3, SnO, $SrCO_3$, Nd_2O_3, and Nb_2O_5 (all from Sigma Aldrich having purity of more than 99.5%) were extensively wet milled for 22 hours using silicon carbide balls in a Retsch PM 200 planetary ball mill using hard tungsten carbide balls of diameter 5 mm and the ball to powder mass ratio was considered 10:1. A 30-minute break (pause time) was taken into consideration after every two hours of wet milling in an ethanol solution at 300 RPM. Obtained sullery was further mixed with the right amount of Polyvinyl Acetate (PVA) binder and compressed into a cylindrical pallet having a diameter of 10.8 mm and thickness of 2 mm. Further, the pallets were sintered in an alumina crucible at 1000 ^OC for 4 hr. in a microwave furnace having a frequency of 3.5 GHz.

2.2 Characterization techniques

The crystal structure of the prepared NdSBN ceramics was examined using Bruker D8 DISCOVER equipped with Cu-Kα radiation (λ = 1.5406 nm), operated at (40 kV and 40 mA). The crossectional surface morphology was investigated using Carl Zeiss Merlin VP Compact FE-SEM with 5KV acceleration voltage and 100 K magnification. Cross sectional SEM is used with the premise that it provides information about the uniformity, thickness, and quality of each layer, which is vital for understanding the material's overall performance. Additionally, the cross-sectional measurement aids in the detection of voids, fractures, and other faults in the composition; determining the presence of these defects is essential for assessing the material’s reliability and predicting failure mechanisms. For the electrical measurements, the pellets were coated with the silver paste and cured at 350 ^oC for 30 min. DC conductivity was measured using a Keithley 6517B high resistance

meter/Electrometer in a temperature range of 30 to 710 ºC. Frequency and temperature-dependent AC conductivity, dielectric, impedance, Curie temperature, and modulus spectroscopy were investigated by employing ZM2376 (NF corporation, Japan), high frequency LCR meter with an applied oscillation level voltage of 1V.

3. Result and discussion

3.1 Structural and Phase Analysis

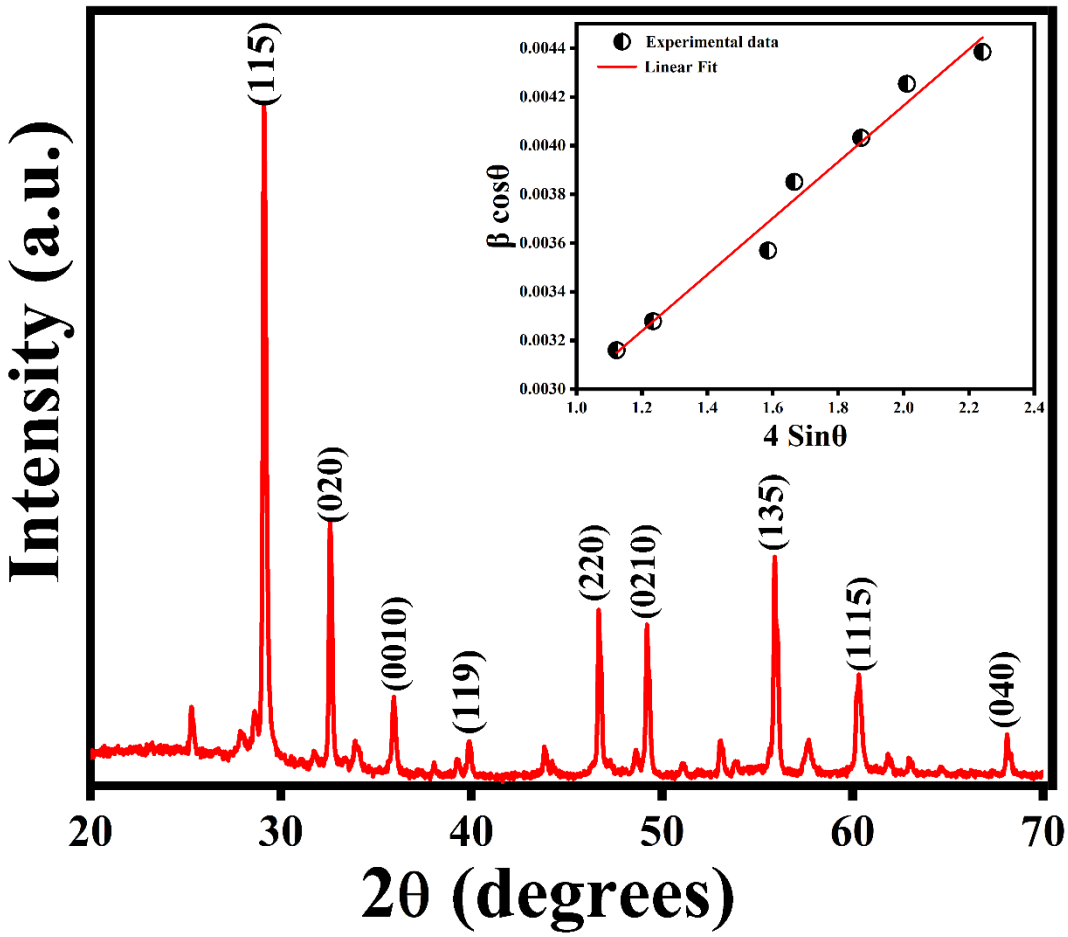


Figure 1 Room temperature XRD pattern of Nd doped SBN ceramics, Inset shows the Williamson Hall (W-H) plot of the same.

Fig.1 shows the room temperature X-ray diffraction (XRD) pattern of microwave sintered $Sr_{0.8}Sn_{0.2}Bi_{1.75}Nd_{0.25}Nb_2O_9$ ceramics at 1000 ºC for 4 hr. A close examination of XRD pattern reveals a single-phase orthorhombic crystal structure with $A2_1am$ space group. A well-defined sharp peak was observed, implying a high degree of crystallinity in the NdSBN solid solution. A few impurity peaks were also observed in the XRD which corresponds to the presence of an unreacted mixture in the solid solution. The most intense peak (115) in the XRD pattern indicates that NdSBN ceramic is double layered Aurivillius phase with the most intensive reflection of the type (112m+1) plane. The Lattice parameter and volume were computed using JCPDS card no 49-0607 and, 37-1493, resulting in approximately 5.513 Å, 5.522 Å, 25.146 Å, and 765.514 $Å^3$. To acquire additional crystallographic information, the obtained XRD pattern was extensively examined using Rietveld refinement performed using full prof software. Several profile fitting parameters R_p (profile

factor), R_{wp} (weighted profile factor), and R_{exp} (expected weighted profile factor) make it handy to know the crystallographic properties and are displayed below.

$$\Delta = \sum_i W_i\{I_{io} - I_{ic}\}^2 \quad \text{..... (1)}$$

$$R_p = \frac{\sum_i |I_{io} - I_{ic}|}{\sum_i I_{io}} \quad \text{..... (2)}$$

$$R_{wp} = \left[\frac{\sum_i W_i (I_{io} - I_{ic})^2}{\sum_i W_i \{I_{io}\}^2}\right]^{1/2} \quad \text{..... (3)}$$

$$R_{exp} = \left[\frac{n-p}{\sum_i W_i \{I_{io}\}^2}\right] \quad \text{..... (4)}$$

Where W_i is the weight parameter I_{io} and I_{ic} are observed and calculated intensity, n is the total number of experimental points and p is the number of refined parameters[22, 23].

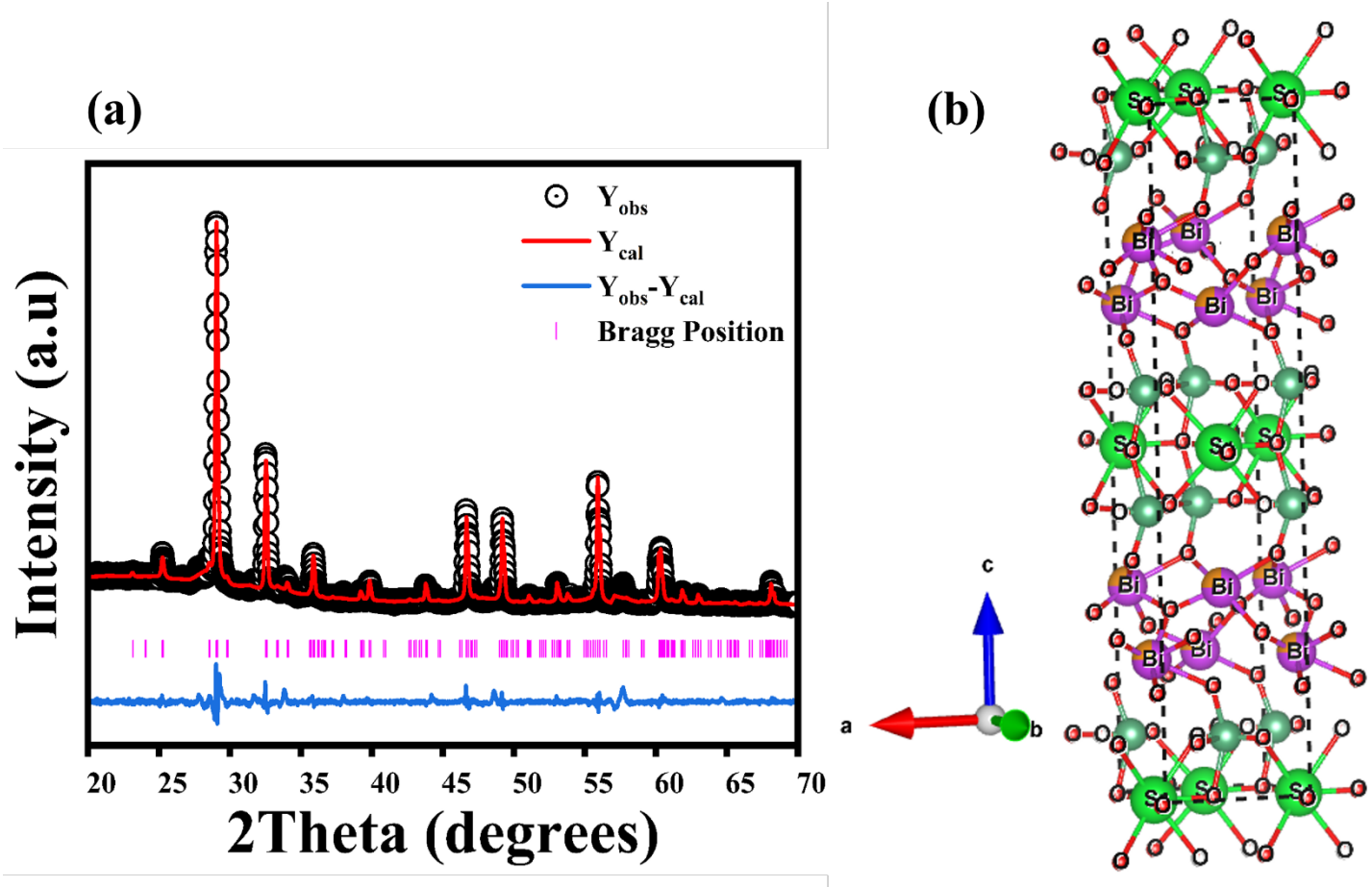


Figure 2(a) Rietveld refinement profiles of NdSBN ceramic carried out through Full prof software (b) Crystal structure of NdSBN ceramic drawn from VESTA software.

Fig.2(a) and **2(b)** depict the Rietveld refined patterns and crystal structure of polycrystalline $Sr_{0.8}Sn_{0.2}Bi_{1.75}Nd_{0.25}Nb_2O_9$ ceramics respectively**.** An Exceptional fitting can be clearly illustrated from the tight overlap between calculated and observed intensity values, which further strengthens the hypothesis of

perfect substitution in the parent SBN ceramics. The acquired lattice parameters and other information from Rietveld refinement are summarized in **Table 1**.

Table 1 Rietveld refinement results of NdSBN ceramic sample obtained from XRD data.

Parameters	**$Sr_{0.8}Sn_{0.2}Bi_{1.75}Nd_{0.25}Nb_2O_9$ (NdSBN)**			
Space group	$A2_1am$ (Orthorhombic)			
Cell Parameters (Å)	5.5025, 5.5013, 25.0200			
Unit cell volume ($Å^3$)	757.386			
Density (g/cm^3)	7.534			
Chi-square (χ^2)	3.76			
GOF	1.9			
Bragg R–factor (%)	6.68			
R–factor (%)	5.18			
Conventional R–factors (%)	7.43			
R_p	27.1			
R_{wp}	21.9			
R_{exp}	11.28			
Atomic Positions	**Elements**	**X**	**Y**	**Z**
	Sr1	0.50026,	0.25812	0
	Sn1	0.50026	0.25812	0
	O1	0.68572	1.74923	0.91341
	Bi1	1.02058	0.76578	0.20116
	Nd1	1.02058	0.76578	0.20116
	O2	1.06097	0.68701	0.34101
	O3	1.27382	0.45888	0.26559
	O4	1.06869	0.23527	0.00000
	O5	1.27104	1.42395	0.58342
	Nb1	1.00092	0.75053	0.41394

3.2 Crystallite size and strain determination

X-ray peak profile analysis (XPPA) is a compelling technique to calculate the crystallite size along with the lattice strain of the system. Peak broadening in any materials (film, bulk, nanocrystals, etc.) mostly arises due to two major components, intrinsic strain effect and crystalline size effect. This peak broadening usually comprises of two major components physical dislocation and instrumental effects, which can be corrected by the eqn.5 [24].

$$\beta_d^2 = [\beta_{measured} - \beta_{instrumental}]^{1/2} \quad \ldots\ldots\ldots\ldots\ldots (5)$$

Here, β_d, $\beta_{measured}$ and $\beta_{instrumental}$ are the corrected broadening, measured broadening, and instrumental broadening respectively. The instrumental broadening and position calibration were performed by collecting the diffraction data of standard material, usually, the crystalline silicon has been used for this purpose. Further, the corrected physical broadening and instrumental broadening of the sample were estimated by FWHM (Full-width half maxima), which is used to calculate the average particle size of the composition using Debye Scherrer's equation depicted below[25, 26].

$$\boldsymbol{D} = \frac{0.9\,\lambda}{\beta\cos\theta} \quad \text{.................................} \quad (6)$$

Where D, denotes the crystallite size, λ is the wavelength of X-ray (1.5406 Å), and β is the FWHM. The estimated crystallite size comes around 60.5 nm.

While analyzing the XRD peak broadening the DS method solely considers the contribution from crystallite size, while ignoring the lattice strain contribution. Nevertheless, the Williamson Hall (W-H) method can be used to address this issue as it acknowledges the contribution from both strain driven peak deformation and crystallite size on peak broadening. Thus, the total peak broadening can be written as

$$\boldsymbol{\beta_{hkl}} = \boldsymbol{\beta_{size}} + \boldsymbol{\beta_{strain}} \quad \text{..} (7)$$

Where β_{hkl} represents the FWHM of an XRD peak, and β_{size} and β_{strain} are the widths due to the size and strain, respectively. Uniform Deformation Model (UDM), states that the strain is isotropic, which arises in the crystalline structure due to imperfections[24]. The strain-influenced peak broadening is shown in eqn.8,

$$\boldsymbol{\beta_{strain}} = 4\varepsilon\tan\theta \quad \text{.......................................} \quad (8)$$

On rearranging the eqn. 5, 6, 7, and 8, we get

$$\boldsymbol{\beta_{hkl}} = \frac{K\,\lambda}{D.Cos\,\theta} + 4\varepsilon tan\theta \quad \text{............................} (9)$$

$$\boldsymbol{\beta_{hkl}}\,\mathbf{Cos}\theta = \frac{\boldsymbol{K\,\lambda}}{\boldsymbol{D}} + \boldsymbol{4\varepsilon Sin}\theta \quad \text{..............................} \quad (10)$$

Eqn.10, known as the UDM equation, indicates the isotropic nature of the crystals, where D and ε are crystallite size and microstrain, respectively[25, 27, 28]. **Inset of Fig.1** shows the W-H plot of NdSBN ceramics. The estimated value of crystallite size is around 80 nm and generates a strain of roughly $1.16x10^{-3}$.

3.3 Morphological Analysis

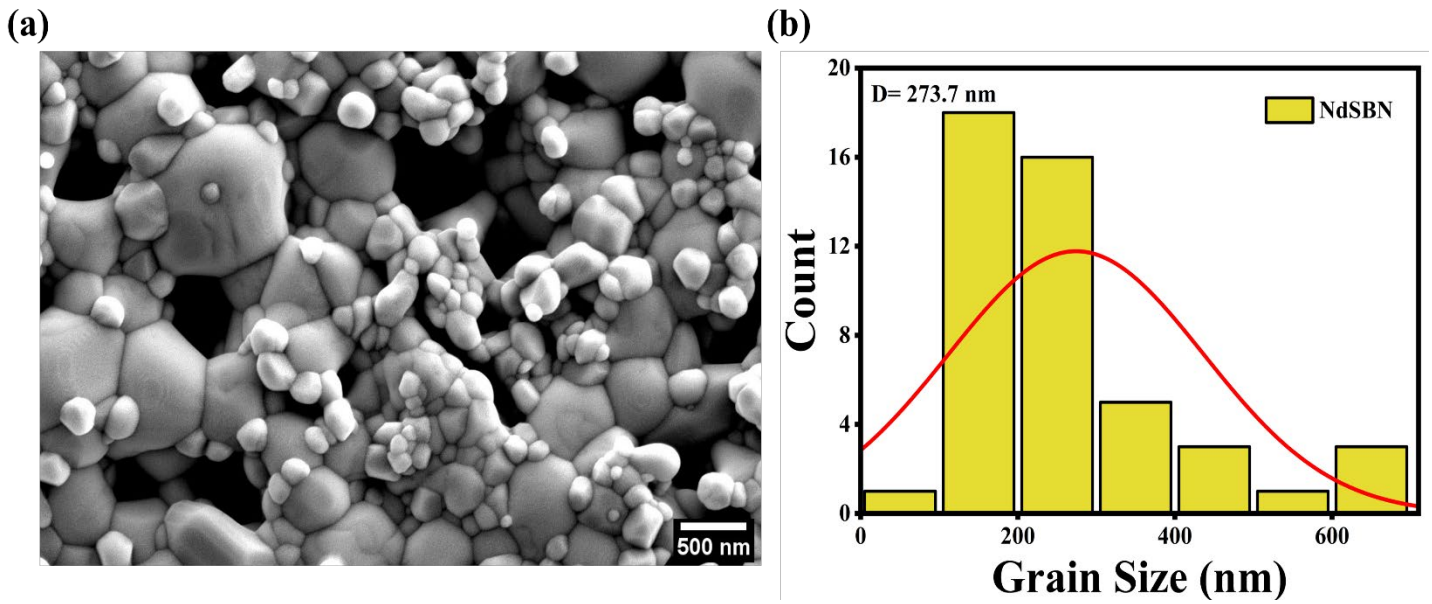


Figure 3 (a) Crossectional SEM micrograph of microwave sintered NdSBN ceramics (b) The grain size distribution along the length direction of different components.

The cross-sectional SEM morphology of microwave sintered NdSBN ceramics is shown in **Fig. 3(a)**. The morphology consists of the distinct, compact large and small grains interconnected with grain boundaries and makes an appealing and rare microstructure [5]. The variation in the size of the grains indicates the polycrystalline nature of the prepared NdSBN ceramics [29, 30]. The SEM morphology exhibits distinct asymmetric sizes of voids and porosity, which primarily arises due to the volatile nature of bismuth at elevated temperatures. However, the PVA binder evaporation, impurities, and oxygen vacancies can also be contributing factors for the same. The average grain size was determined using Image J software with a scale of 500 nm and magnification of 50 KX. Normal distribution curve fitting of the histogram was employed to calculate mean grain size of the composition, which is approximately 273.7 nm, shown in **Fig.3(b)** [2].

3.4 Dielectric Spectroscopy

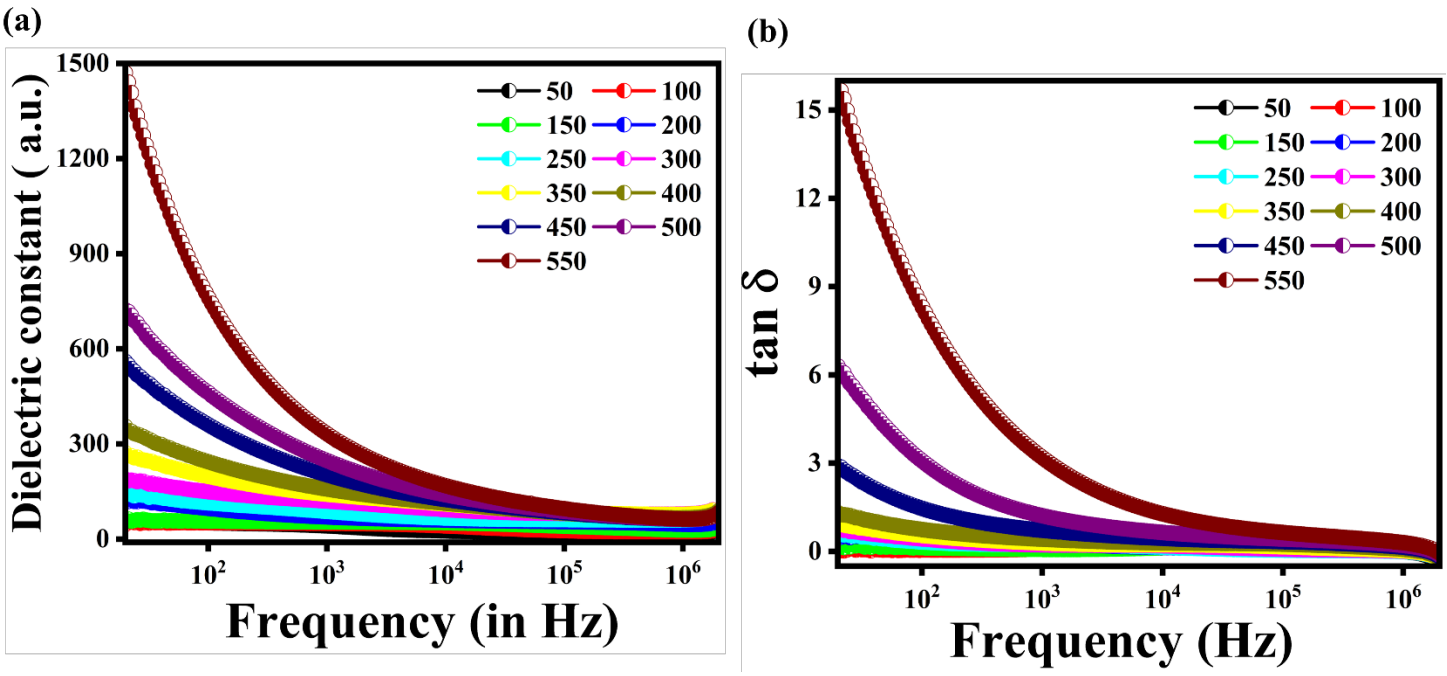


Figure 4 Frequency dependent variation of (a) Dielectric constant (b) dielectric loss at several temperatures of NdSBN ceramics.

Frequency dependent variation of dielectric constant at several temperatures is shown in **Fig. 4(a).** It was observed that the dielectric constant decreases with the increase in frequency and stabilizes further, this type of behavior primarily arises from the combined effects of extrinsic and intrinsic polarization. Extrinsic polarization occurs due to sample microstructure, dislocation of charges, defects, electrode contribution, and Maxwell-Wagner effect. In contrast, intrinsic effect arises due to different kinds of polarization, Electronic, Ionic, Orientational, and Space charge polarization, commonly observed in Aurivillius layered materials[4, 31]. The dielectric loss or loss tangent is defined as the ratio of real and imaginary components of dielectric constant of any material at any given temperature. The variation of loss tangent at various temperatures is shown in **Fig. 4(b)**. A substantial dielectric loss is observed at low frequency and high temperatures, which is consistent with our conductivity analysis and may arise due to leakage current and conductivity-based loss.[32–34]. On the other hand, at high frequencies the grains exhibit a lesser resistance, which significantly reduces the energy needed by the charge carrier for motion, thus resulting in a low dielectric loss[35].

3.5 Curie Temperature Analysis

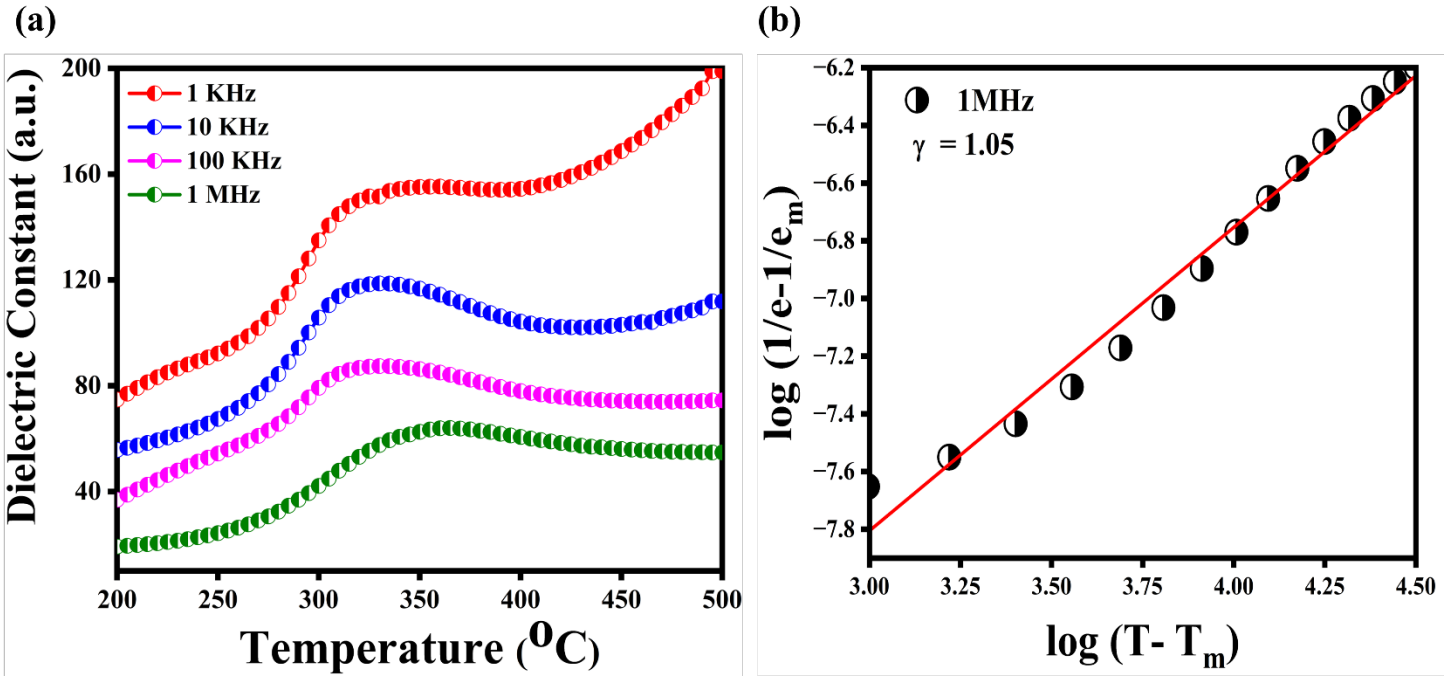


Figure 5 (a)Temperature dependent variation of dielectric constant of NdSBN at several frequencies (b) fitting to Curie-Wiss law of NdSBN ceramics at 1MHz.

The temperature dependent dielectric investigation of NdSBN ceramics is shown in **Fig. 5(a).** The dielectric constant is displayed as a function of frequency from 1 KHz to 1 MHz, in a temperature range of 25 °C–550 ◦C. A distinct ferroelectric to paraelectric phase transition was observed in all measurements, arising due to short-range ordering, presence of polar nano regions, composite fluctuations, and structural distortion. The Curie temperature was found to lie in a temperature range of 330 to 340 °C, which is lower than the reported value of SBN, possible reason accounting for the same is the decreased tetragonal strain in the NdSBN ceramics and size-dependent electronic polarization [2, 6, 36]. This decrease in Tc is also associated with the change in Nb–O-Nb angles, suggesting a lesser rattling space for Nb ions in the NbO_6 octahedron, which diminishes the ion shifts [4]. A broad peak was observed for all measurements, demonstrating a diffuse type phase transition. Additionally, the Uchino and Nomura function, a modified version of Curie-Weiss law (CW) was used to investigate the diffuseness of a relaxor ferroelectric ceramics, depicted in eqn.11.

$$\frac{1}{\varepsilon} - \frac{1}{\varepsilon_m} = \frac{(T-T_m)^{\gamma}}{C} \quad \text{..... (11)}$$

Where ε_m is the maximum value of dielectric constant at temperature T_m, C is the Curie constant and γ is a degree of diffuseness of phase transition, whose value lies between 1 to 2, and represents normal and relaxor ferroelectrics respectively[36, 37]. The plots of log $(1/\varepsilon - 1/\varepsilon_m)$ as a function of log $(T- T_m)$ at 1MHz for NdSBN ceramics are shown in **Fig. 5(b)**. The experimental data are fitted with the least square function and the slope of this plot gives the value of γ. For all measurements, the value of γ ranges between 1.05 to 1.2.

AC Conductivity Measurement

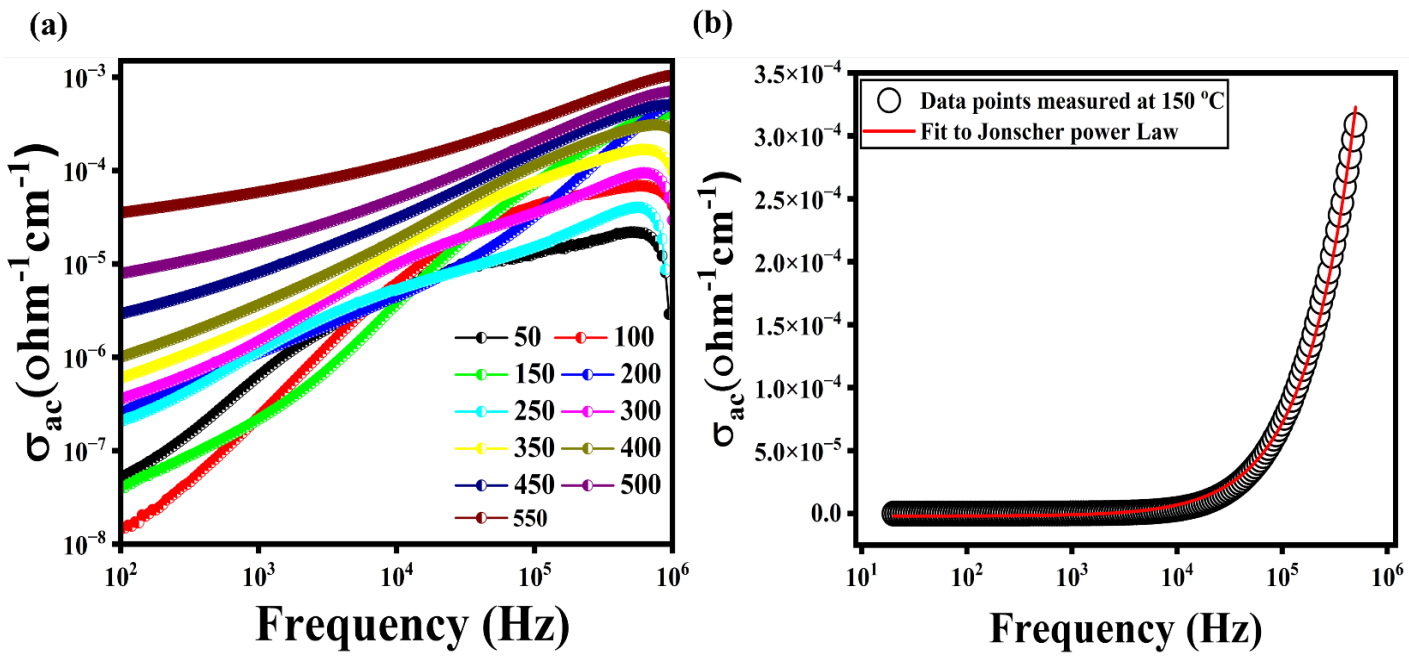


Figure 6 (a) Frequency dependent variation of AC conductivity of NdSBN ceramics at several temperatures (b) fitting of Jonscher's power law to the experimental data at 150 °C.

AC conductivity in a solid is a thermally governed process, in which the charges migrate sequentially under the effect of an applied external electric field. The frequency dependent AC conductivity of solid is calculated using eqn.12.

$$\sigma_{ac} = 2\pi f \varepsilon_o \varepsilon' tan\delta \quad \text{.....(12)}$$

where the f, ε', tanδ and ε_0 are the frequency, dielectric permittivity, dielectric loss, and permittivity of free space respectively. **Fig.6(a)** shows the frequency-dependent AC conductivity plot of NdSBN ceramics at variable temperatures. The conductivity plot can be differentiated into two distinct regions: the first one is a low frequency regime in which, a plateau like region is observed where the conductivity is independent of frequency and resembles to DC conductivity of the ceramics, suggesting a long range transport mechanism in the system. The second one is high frequency regime, where conductivity is frequency dependent and increases with it until it exhibits a dispersion behavior, irrespective of temperatures [23, 38]. Nevertheless, an increase in conductivity is also observed with the increasing temperature, which may be due to a polaron hopping assisted conduction mechanism in the solid. One might gain a deeper understanding of ac conductivity by examining it using Jonscher's Power Law shown in eqn.13.

$$\sigma = \sigma_{d.c.} + A\omega^s \quad \text{..... (13)}$$

where σ is the total conductivity of the system, $\sigma_{d.c.}$ is the conductivity affecting the frequency-independent direct current part, A is a pre-exponential factor that governs the strength of polarizability, ω is the angular frequency, and 's' is a dimensionless exponent that articulates the degree of interaction between surrounding lattice and mobile ions, typically lies between 0 to1. The s <1 indicates the translational motion of the charge

carrier and s >1 depicts the localized motion[9, 29, 31]. According to Jonscher's power law, the frequency dispersion driven conductivity develops particularly due to the relaxation of the mobile charge. **Fig. 6(b)** shows Jonscher's fitting of experimental conductivity data of NdSBN ceramics at 150 ºC. Our investigation revealed that the 's' rises with the increasing temperature till 300 ºC and decreases thereafter depicted in **Table 2.** This suggests that the hopping conduction in NdSBN ceramics was aided by the presence of a charge carrier [2, 31].

Table 2 Variation of dimension less exponent ('s') with temperature for NdSBN ceramics.

Temp.	50	100	150	200	250	300	350	400	450	500	550
s	0.31	0.52	0.62	0.53	0.53	0.55	0.58	0.62	0.65	0.67	0.76

3.6 DC Conductivity Analysis

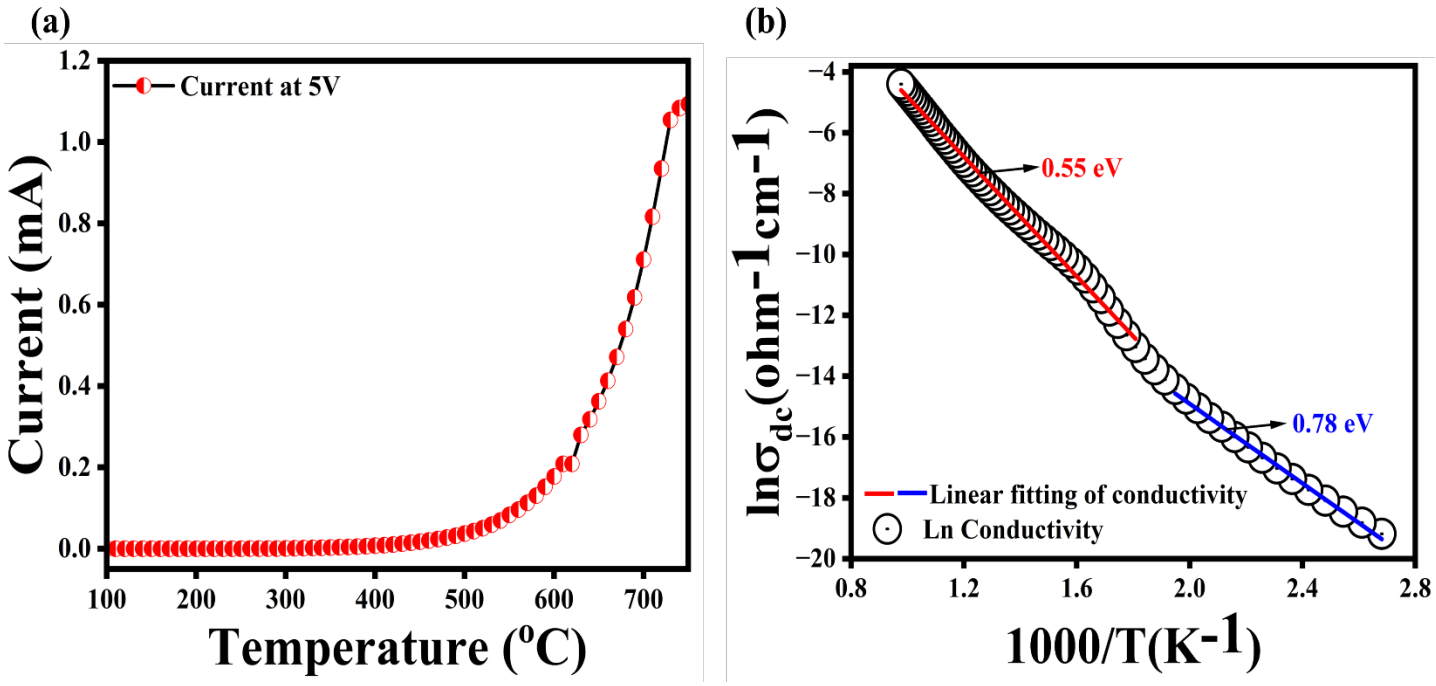


Figure 7 (a) DC Conductivity measurement of NdSBN ceramics at 5V (b) Arrhenius plot of the obtained DC conductivity

Conductivity study not only provides us with information on the nature of charge carriers involved in the conduction process but also provides insight into the impression of conductivity on the domain structure and its motion[39]. The temperature dependent ionic DC conductivity of NdSBN ceramics is shown in **Fig. 7(a).** Thermally excited charge carriers migrate to the conduction band and exhibit an increase in conductivity with the increasing temperature which corresponds to the mobile oxygen ions in the paraelectric phase [40]. The minimum energy necessary for the mobility of vacancies determines the conductivity of materials and is known as activation energy, which can be further determined using the Arrhenius equation shown below.

$$\boldsymbol{\sigma_{dc} = \sigma_o e^{\left(\frac{-E_a}{K_b T}\right)}} \ldots\ldots\ldots\ldots\ldots\ldots\ldots\ldots \text{(14)}$$

Where σ_o is the pre-exponential factor, E_a is activation energy, K_b is Boltzmann constant, and T is the absolute temperature. **Fig.7(b**) illustrates the presence of two distinct DC active zones with activation energies (E_a) of 0.55 eV and 0.78 eV, indicating the existence of independent electronic and ionic thermal regions. Higher E_a value is due to the high polarizability of bismuth cations which primarily results from the dominance of the free charge associated with oxygen anions and eventually impedes its movement in oxygen sublattice under the action of applied DC fields [23, 30]. Additionally, the long range polaron hopping also contributes effectively to the same. [31].

3.7 Impedance Spectroscopy

Understanding the effects of grain, grain boundary, and electrode effect in solids is vital because these factors significantly impact the electrical properties of dielectric and ferroelectric materials. However, probing these effects in a solid is a challenging task and needs sophisticated techniques. Complex impedance spectroscopy (CIS) has proved to be the most suitable technique for this work as it provides information on the individual contribution of several processes to the electrical behavior of the solid at specific frequencies and temperature[23, 41]. The primary advantage of complex impedance spectroscopy is its emphasis on the highest resistance part, whereas complex modulus spectroscopy (CMS) emphasizes the smallest capacitance in the solids[42].

The classical model of impedance spectroscopy is depicted below.

$$\boldsymbol{Z^*} = - i\omega C_o \varepsilon^* \ldots\ldots\ldots\ldots\ldots\ldots\ldots\ldots\ldots\ldots \text{(15)}$$

Z* can be further resolved in real (Z') and imaginary part (Z") of impedance and shown below.

$$\boldsymbol{Z'} = \frac{1}{2\pi f C_o}\left[\frac{\varepsilon''}{\varepsilon'^2 + \varepsilon''^2}\right] \ldots\ldots\ldots\ldots\ldots\ldots\ldots\ldots \text{(16)}$$

$$\boldsymbol{Z''} = \frac{1}{2\pi f C_o}\left[\frac{\varepsilon'}{\varepsilon'^2 + \varepsilon''^2}\right] \ldots\ldots\ldots\ldots\ldots\ldots\ldots\ldots \text{(17)}$$

Where f is frequency, ε' and ε" are real and imaginary parts of the dielectric constant, and C_o is the capacitance of vacuum[43].

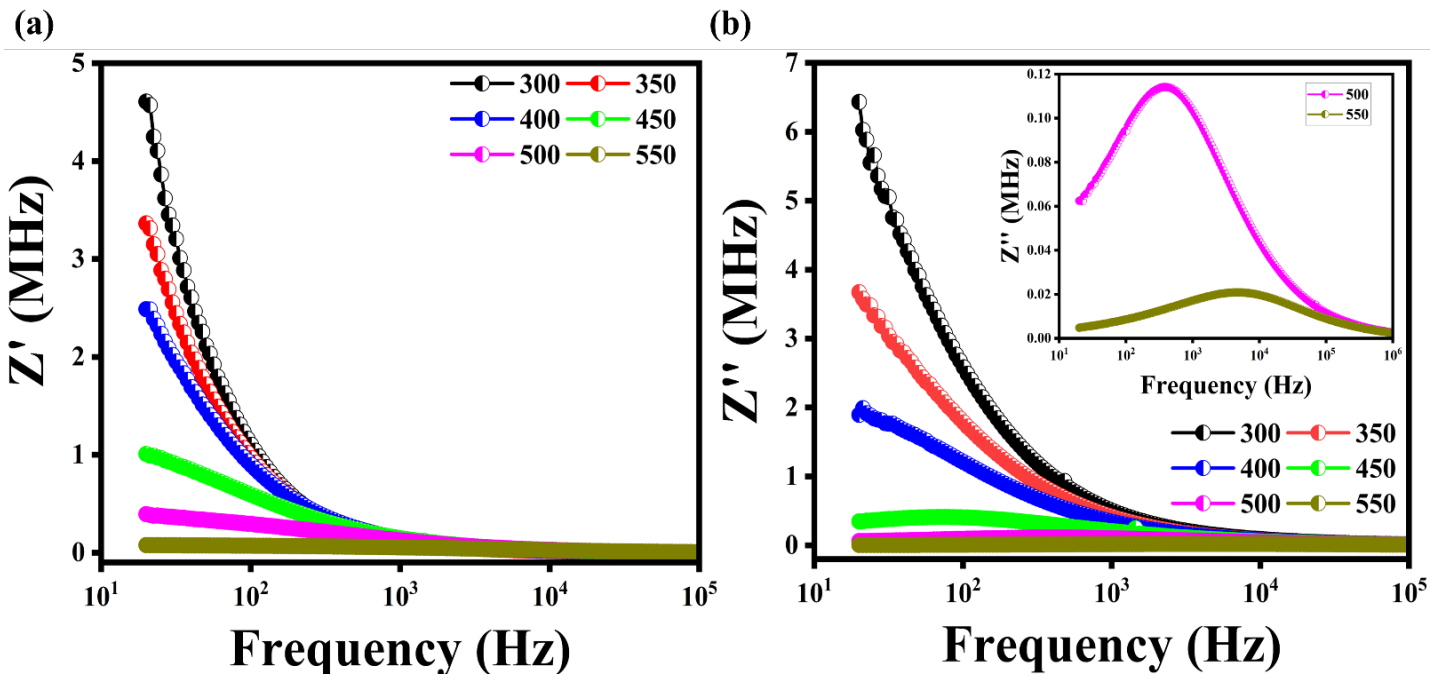


Figure 8 Variation of (a) Real and (b) imaginary part of complex impedance as a function of frequency at different temperatures.

Fig. 8(a) shows the frequency dependent variation of real part of impedance (Z') at several temperatures. It suggests that the Z' decreases with the decreasing frequency, pointing towards the increase in the conduction in the NdSBN ceramics. A high value of Z' is observed in a high frequency region, possibly due to contribution from all four types of polarization. Additionally, it has been observed that the Z' decreases with increasing temperature, suggesting negative temperature coefficient of resistance (NTCR) behavior which illustrates the presence of semiconducting properties in the NdSBN ceramics [2, 13]. Eventually, the Z' merges in a high frequency region regardless of temperature, demonstrating a further lowering of the potential barrier [44]. The frequency dependent variation of imaginary part of impedance (Z'') at variable temperatures is shown in **Fig. 8(b)**. A swift decrease in the value of Z'' with the increasing frequency is observed depicting a non-Debye type relaxation mechanism. The broadening of Z'' peak indicates multiple relaxation mechanisms in the NdSBN ceramics, which arise due to the existence of defects at higher temperatures and static charge species at lower temperatures. A decrease in the amplitude of Z'' peak is observed with the increasing temperature (shown in the inset of **Fig. 8(b))**, implying that the electrical process is dominated by space charge polarization, which is known to exist in the heterogeneous structures [23, 43]. Ultimately all curves merge in high frequency regions, (typically above 10^5 Hz), possibly due to short relaxation time of the space charge at high frequencies, in due course reducing the system's net space charge polarization. Moreover, the Z'' peak shifts towards high frequency region indicating a thermally activated relaxation mechanism in microwave sintered NdSBN ceramics.[41, 44].

3.8 Cole-Cole Plot

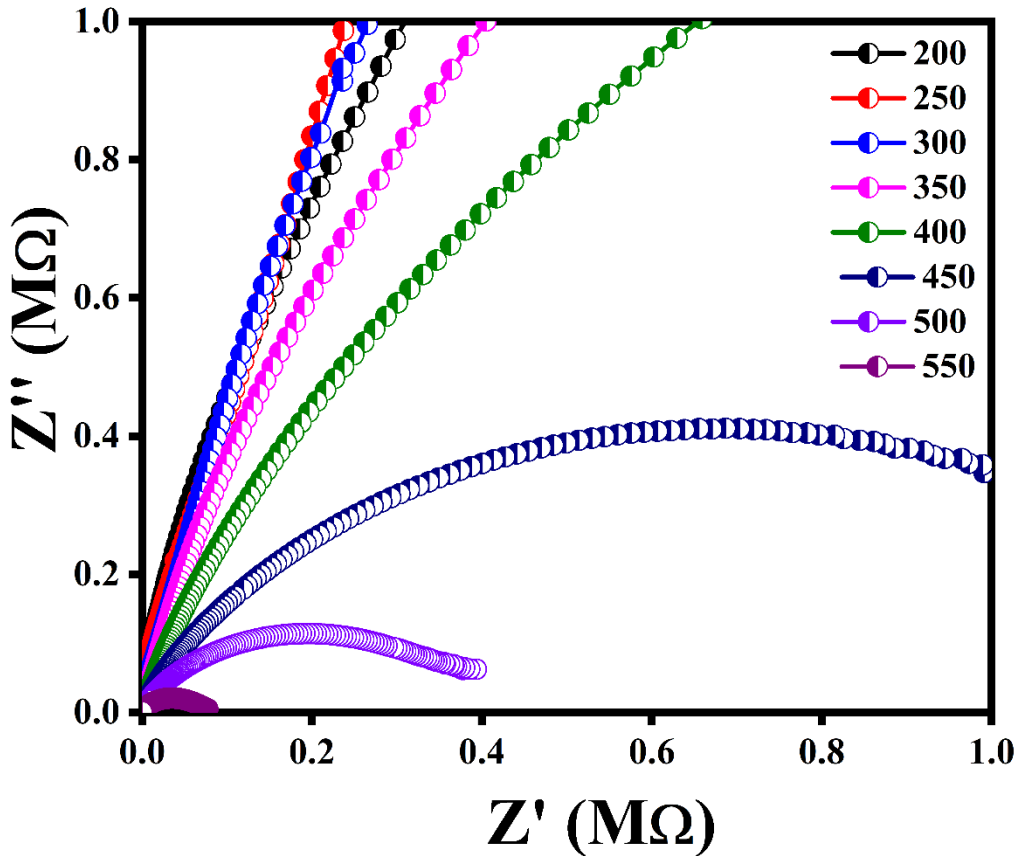


Figure 9 Cole-Cole Plot of NdSBN ceramics at different temperatures

The Cole-Cole plot distinguishes between the resistive and capacitive behavior of grain and grain boundary. Typically, it exhibits one to three successive semicircular arcs, suggesting the number of electrically active regions in the material. The first semicircular arc represents the grain contribution, which is typically observed in high frequency regions, whereas the second and third semicircular arcs indicate grain boundary and electrode contribution respectively, primarily occur in low-frequency regions [2, 41, 43]. **Fig.9** depicts the Cole-Cole plot of the NdSBN ceramics in a temperature range of 200 to 550 ^{o}C. At temperatures below 350 ^{o}C, the response of the Cole-Cole plot was found to be linear, which depicts the insulating or resistive behavior of the NdSBN ceramics, however beyond 350 ^{o}C the linear behavior started to transform into a semicircular one indicating the increase of conductivity in prepared solid solution [42, 45]. A single semicircular arc was observed in all measurements, illustrating the dominance of grain contribution, in contrast, the absence of second and third semicircles ruled out the grain boundary and electrode contribution. The radius of semicircles decreases drastically with the increase in temperature, illustrating the presence of a thermally activated conduction process in the material. Additionally, it was also observed that the center of the semicircles lay below the real axis, indicating that the NdSBN ceramics exhibit non-Debye type behavior.[13, 31].

3.9 Complex Modulus Spectroscopy

Complex modulus spectroscopy (CMS) is a powerful technique first introduced by Macedo et al. to examine the dynamical aspects of the electrical transport property of the ionic solid, such as relaxation mechanism, ion hopping rate, conduction process, and many more [2, 9, 31]. However, CMS also plays a significant role in investigating the spectral components of solids having equivalent resistances but different capacitances, which can be clearly understood by the fact that at lower frequencies the contribution from the electrode polarization effects is strongly concealed [5, 16, 34]. CMS can be mathematically expressed in eqn.18.

$$M^* = \frac{1}{i\omega C_o Z^*} \quad \ldots\ldots\ldots\ldots\ldots\ldots\ldots\ldots\ldots\ldots \quad (18)$$

$$M^* = M' + iM''$$

further M* can be resolved into real (M') and imaginary components (M'') are depicted below.

$$M' = \frac{\varepsilon'}{\varepsilon'^2 + \varepsilon''^2} \quad , \quad M'' = \frac{\varepsilon''}{\varepsilon'^2 + \varepsilon''^2} \quad \ldots\ldots\ldots\ldots\ldots\ldots\ldots\ldots\ldots\ldots \quad (19)$$

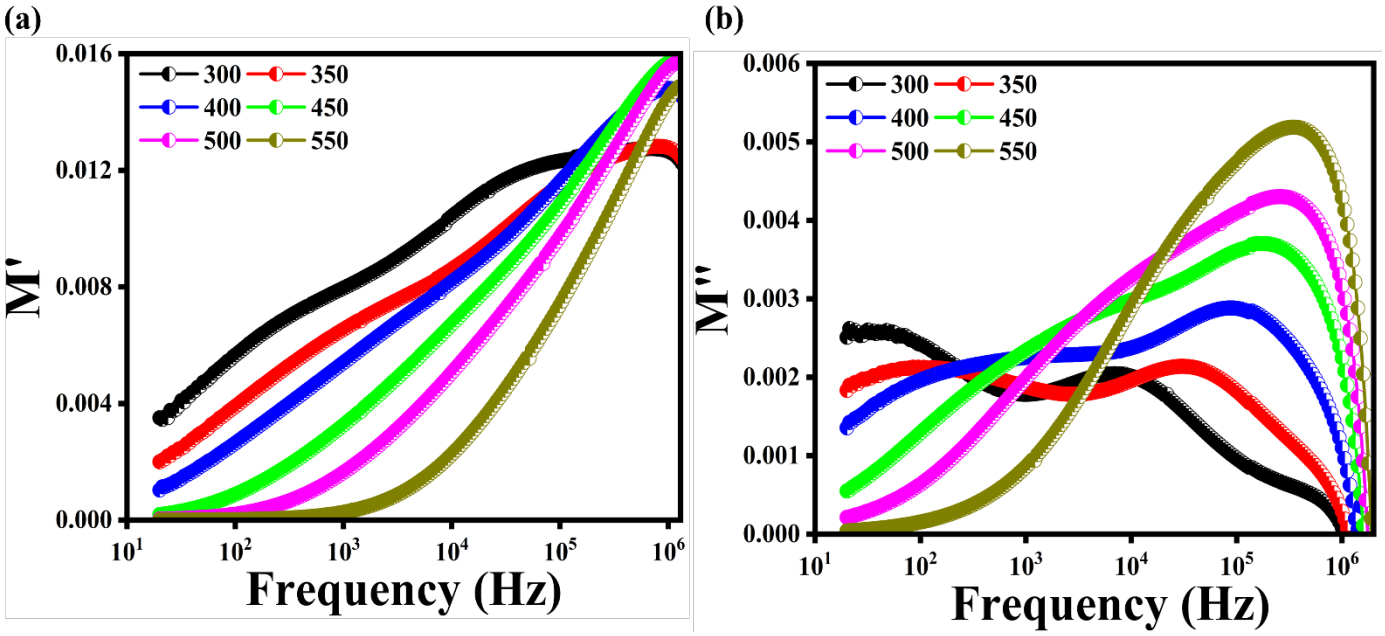


Figure 10 Variation of (a) Real and (b) imaginary part of complex modulus as a function of frequency at different temperatures.

Fig.10(a) and **10 (b)** represent the frequency dependent real (M') and imaginary (M'') components of complex modulus spectroscopy of microwave sintered NdSBN ceramics at variable temperatures. **Fig.10(a)** indicates that the value of M' approaches zero in the low frequency region, thus suggesting an absence of electrode polarization in the NdSBN ceramics. However, a gradual increase in the value of M' is observed with the increase in frequency, which eventually attains a saturation point, suggesting a short-range mobility of charge carrier clubbed with the enhanced orientational polarization in the system [5, 31, 46]. **Fig. 10(b)** indicates an increase in M'' with the increasing frequency eventually attaining a maximum at a specific frequency known as most feasible conductivity relaxation frequency. With the increasing temperature the peak of M'' shifts towards high frequency region, suggesting that the dielectric relaxation mechanism is a thermally activated

process in which the hopping of the charge carrier is intrinsically dominated. All measurements display an asymmetric broadening of M" peak, indicating a non-Debye-type relaxation process with variable time constants [2, 35, 42].

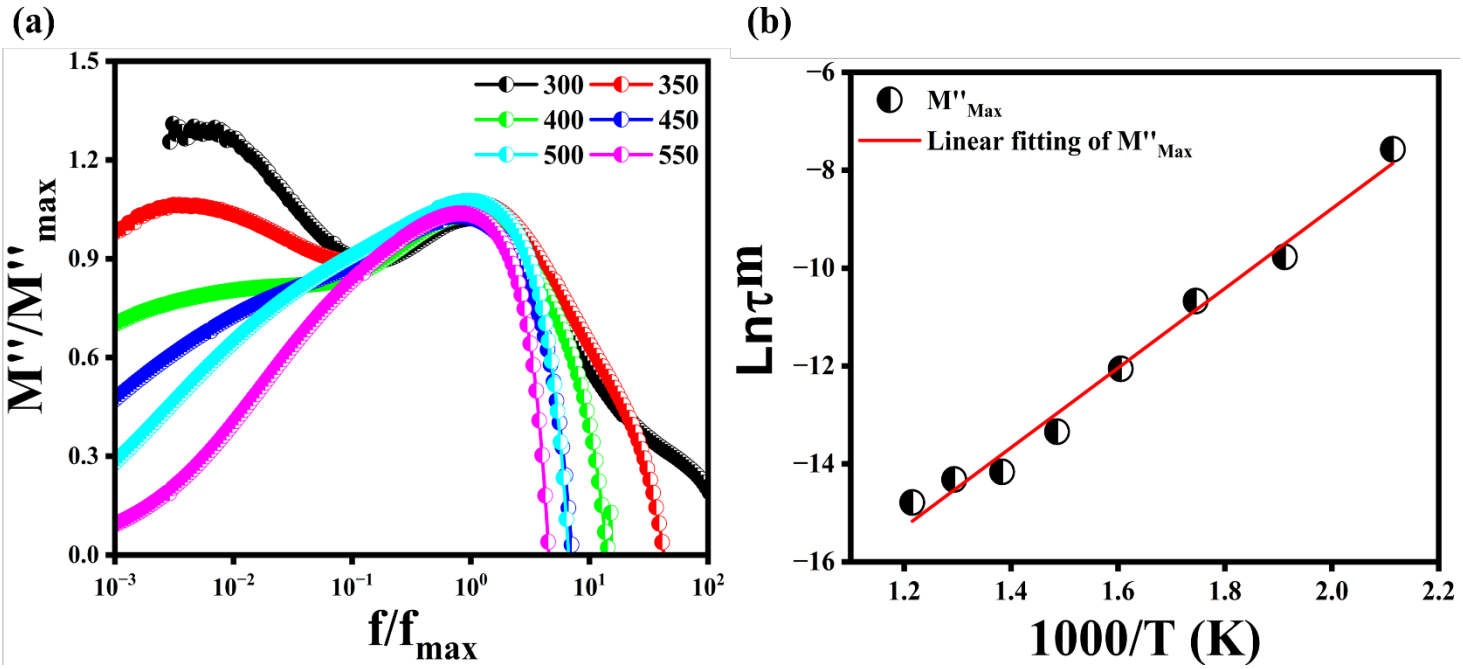


Figure 11 (a) Scaling behavior of M''/M''max as a function of f/fmax of NdSBN ceramics at different temperatures (b) ln (τ^m)as a function of 1000/T of NdSBN ceramics.

The scaling behavior of NdSBN ceramics with the plot of normalized M''/M''_{max} as a function of f/f_{max} at different temperatures is depicted in **Fig.11(a).** All peak collapses in a bigger curve known as master module curve, which provides an apparent picture of how the dielectric mechanism within the solid functions. As temperature rose a transition from long-range to short-range motion was observed [27, 39]. **Fig.11(b)** shows the variation of relaxation time(tau) against 1000/T (absolute temperature inverse), from which the dielectric relaxation time can be calculated by the equation depicted below.

$$\tau^m = \frac{1}{\omega^m} \quad \text{..... (20)}$$

$$\tau^m = \frac{1}{2\pi f^m} \quad \text{..... (21)}$$

Where f^m is the relaxation frequency at which the maximum value of M″ was observed, τ^m is the dielectric relaxation time. The relaxation time was further calculated using the Arrhenius equation depicted below.

$$\tau^m = \tau_o e^{\left(\frac{-E_a}{K_b T}\right)} \quad \text{..... (22)}$$

Here τ_o is the pre-exponential factor, E_a is the activation energy of the charge carrier, K_b is the Boltzmann constant (8.6×10^{-5}eV/K) and T is the absolute temperature. The activation energy was found to be 0.69eV, based on the linear fitting of the Arrhenius equation [39, 42].

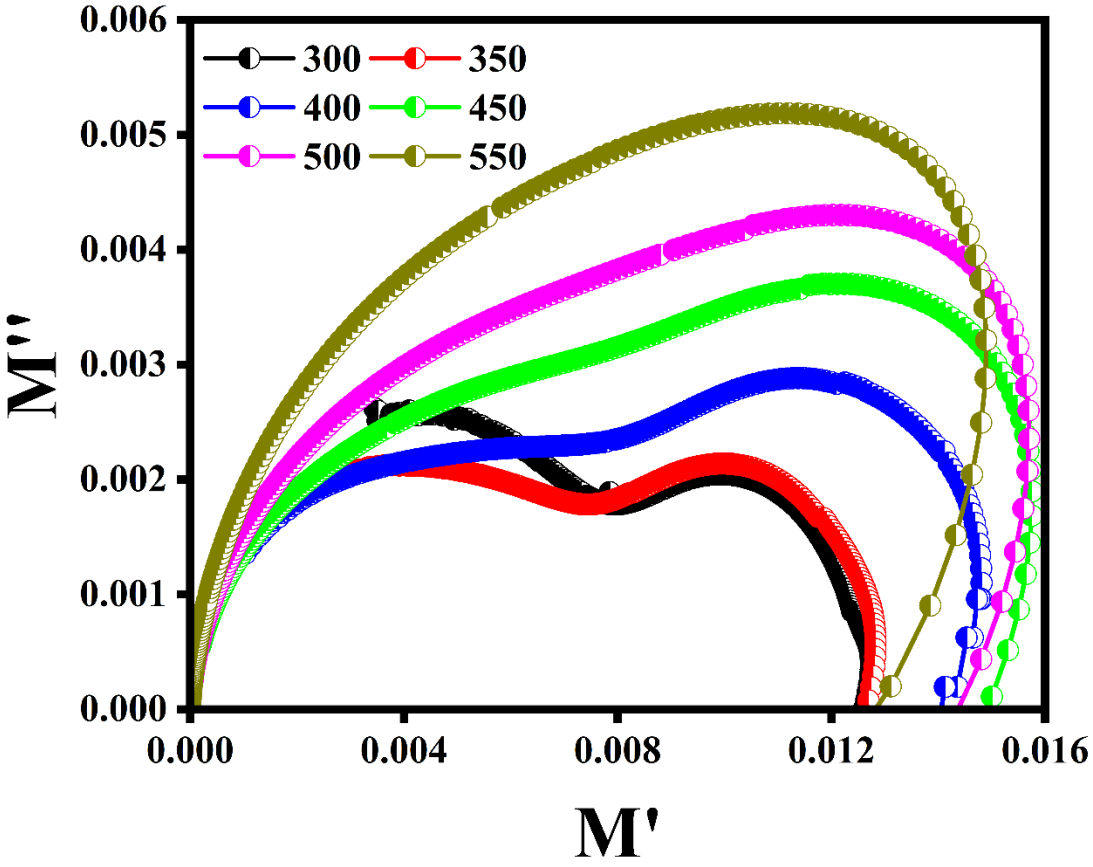


Fig.12 Cole-Cole plot of NdSBN ceramics measured at different temperatures.

Furthermore, the nature of mobile and bound charges at the grain and grain boundary in the solid can be known by plotting the M' vs M'' at selected temperatures depicted in **Fig.12**. Two deformed semicircles were observed for the measurement performed at 300 ºC and 350 ºC, indicating two relaxation processes along with two relaxation time. The smaller semicircle is attributed to the weak grain boundary effect instead of the dominant grain effects, whereas the bigger semicircular arc depicts the grain response. Nevertheless, the measurement carried out beyond 350 ºC reveals a single semicircle arc, which is attributed to grain contribution to the polarization and arises due to dipolar polarization in the prepared NdSBN ceramics [5, 41, 43].

4 Conclusion

In summary, the polycrystalline $Sr_{0.8}Sn_{0.2}Bi_{1.75}Nd_{0.25}Nb_2O_9$ (NdSBN) ceramics were synthesized by conventional solid-state route; however, the incorporation of microwave sintering significantly lowered the processing temperature and time of the same. The orthorhombic phase with $A2_1am$ crystal symmetry is confirmed by room temperature XRD in conjunction with the Rietveld refinement process. However, a few impurities peaks were also found in the XRD pattern, which may be due to the presence of some unreacted mixtures in the NdSBN solid solution. Doping-induced strains and crystallite size were calculated using the UDM model by incorporating Williamson-Hall method, roughly around 1.16×10^{-3} and 80 nm respectively. Cross-sectional SEM reveals the plate-like morphology with an average grain size of 270 nm. Curie temperature measurement indicates a diffuse type phase transition with a broad peak, further the diffuseness of the prepared compositions was investigated using the Uchino and Nomura function, a modified version of Curie-Weiss law (CW). The frequency and temperature dependent dielectric measurement exhibits a

Maxwell-Wagner polarization. Frequency dependent AC conductivity obeys Jonscher's power law, whereas DC conductivity reveals the conductivity in NdSBN ceramics originates owing to long range polaron hopping with an activation energy of 0.55 eV and 0.78 eV, which corresponds to electrons and ions, respectively. Impedance and modulus spectroscopy reveal the non-Debye type relaxation mechanism along with the negative temperature coefficient of resistance (NTCR) behavior. The obtained results support the fact that the NdSBN ceramics can be potentially used as a low-temperature NTC thermistor.

5 Acknowledgement

Anurag Pritam (AP) expresses gratitude towards the Irish Research Council (GOIPD/2023/1225) for providing him with an IRC postdoctoral fellowship at Tyndall National Institute, University College Cork, Ireland. AP also acknowledges the Shiv Nadar Foundation for providing financial assistance during his Ph.D. duration.

6. Author contributions

Anurag Pritam: Conceptualization, analysis, investigation, writing, and editing of the original draft.

7. Conflicts of interest

The author declares that there is no conflict of interest or any personal relationship that could have influenced the work reported in this paper.

8. Data and Code availability

The datasets studied and investigated during the current study are accessible from the corresponding author upon reasonable request, as the experimental data of the current study is confidential and still unpublished.

9. Ethical approval

This work doesn't deal with any experiment regarding embryo and human tissue.

10. References

1. Zhang Y, Xu T, Yu H, et al (2022) Sm-modified bismuth layer-structured SrBi2Nb2O9 multifunctional ceramics with enhanced electrical properties and good photoluminescence properties. Ceram Int 48:18989–18998. https://doi.org/10.1016/j.ceramint.2022.03.182

2. Sahoo RR, Choudhary RNP (2023) Effect of Ce infusion on the structural, dielectric, optical, transport and polarization behavior of Nd-modified triple-layered Aurivillius phase ceramic Bi3NdTi3O12. Ceram Int. https://doi.org/10.1016/j.ceramint.2023.10.095

3. Supriya S (2023) Tailoring layered structure of bismuth-based aurivillius perovskites: Recent advances and future aspects. Coord Chem Rev 479

4. Nagamani S, Nitchal Kiran J, Siva Basivi Reddy B, et al (2022) Dielectric relaxation in layer-structured SrBi2−xGdxNb2O9 (x = 0.0, 0.4, 0.6, and 0.8) lead-free ceramics. Journal of Materials Science: Materials in Electronics 33:12997–13011. https://doi.org/10.1007/s10854-022-08241-6

5. Khopkar V, Sahoo B (2020) Low temperature dielectric properties and NTCR behavior of the BaFe0.5Nb0.5O3 double perovskite ceramic. Physical Chemistry Chemical Physics 22:2986–2998. https://doi.org/10.1039/c9cp05707b

6. Zulhadjri, Wendari TP, Mawardi F, et al (2023) Effect of Gd3+/Ti4+ heterovalent substitution on the crystal structure, morphology, optical properties, and phase transition behavior of bismuth layer-structured SrBi2Nb2O9. J Solid State Chem 319:. https://doi.org/10.1016/j.jssc.2022.123774

7. Kumar N, Shukla A, Kumar N, et al (2018) Structural, electrical and ferroelectric characteristics of Bi(Fe0.9La 0.1)O3. Ceram Int 44:21330–21337. https://doi.org/10.1016/j.ceramint.2018.08.185

8. Kumar N, Shukla A, Kumar N, et al (2021) Eco-friendly Bi(Ni2/5Ti2/5Fe1/5)O3 nanoceramics: Synthesis, dielectric and impedance studies. Ceram Int 47:22147–22154. https://doi.org/10.1016/j.ceramint.2021.04.237

9. Afqir M, Elaatmani M, Zegzouti A, et al (2023) Electrical properties of SrBi2-yYyNb2-xVxO9 (x/y = 0/0, 0/0.2, 0.05/0.1, 0.1/0.05 and 0.2/0) ceramics. Appl Phys A Mater Sci Process 129:. https://doi.org/10.1007/s00339-023-06423-5

10. Mojumdar P, Shaily R, Bokolia R (2021) Structural properties of Strontium Bismuth Niobate (SrBi2Nb2O9) ferroelectric ceramics. In: Materials Today: Proceedings. Elsevier Ltd, pp 4661–4665

11. Fesenko OM, Yaremkevich AD, Tsebrienko T V, et al (2022) Effect of Nb cationic substitution on the microstructure and Raman spectra of SrBi2(Ta,Nb)2O9 thin lms Effect of Nb cationic substitution on the microstructure and Raman spectra of SrBi 2 (Ta,Nb) 2 O 9 thin films. https://doi.org/10.21203/rs.3.rs-2256073/v1

12. Harihara Venkataraman B, Fujiwara T, Komatsu T (2009) Synthesis and characterization of rare-earth doped SrBi2Nb2O9 phase in lithium borate based nanocrystallized glasses. J Solid State Chem 182:1538–1544. https://doi.org/10.1016/j.jssc.2009.04.004

13. Pritam A, Shrivastava V (2019) Hole/electron transport layers in tin-doped SBLN nano materials for hybrid solar cell applications. Journal of Materials Science: Materials in Electronics 30:11054–11062. https://doi.org/10.1007/s10854-019-01447-1

14. Afqir M, Tachafine A, Fasquelle D, et al (2018) Structural and Dielectric Properties of SrBi2−xCexNb2O9 (0 ≤ x ≤ 0.35) Ceramics. J Electron Mater 47:5793–5799. https://doi.org/10.1007/s11664-018-6524-y

15. Afqir M, Tachafine A, Fasquelle D, et al (2018) Dielectric properties of gadolinium-doped SrBi2Nb2O9 ceramics. Journal of Materials Science: Materials in Electronics 29:1289–1297. https://doi.org/10.1007/s10854-017-8034-8

16. Pritam A (2024) Non-debye type conduction mechanism in Gd doped SrBi2Nb2O9 ceramic prepared through single-step microwave sintering method. Materials Science and Engineering: B 303:. https://doi.org/10.1016/j.mseb.2024.117297

17. Joshi S, Shukla A, Kumar N, Choudhary RNP (2024) Nd substitution response on structural, dielectric, and electrical features of bismuth iron titanate. Ceram Int 50:1643–1654. https://doi.org/10.1016/j.ceramint.2023.10.259

18. Thansanga L, Shukla A, Kumar N, Choudhary RNP (2021) Studies of structural, electrical and ferroelectric characteristics of gadolinium and yttrium modified bismuth ferrite. Mater Chem Phys 263:. https://doi.org/10.1016/j.matchemphys.2021.124359

19. Rybakov KI, Olevsky EA, Krikun E V. (2013) Microwave sintering: Fundamentals and modeling. Journal of the American Ceramic Society 96:1003–1020. https://doi.org/10.1111/jace.12278

20. Agrawal D (2010) Microwave sintering of ceramics, composites and metal powders. In: Sintering of Advanced Materials. Elsevier, pp 222–248

21. Joshi A, Shrivastava V, Pritam A (2020) Microwave derived monoclinic Ba1-xSnxNb2O6 materials as an alternative of ITO. J Alloys Compd 828:. https://doi.org/10.1016/j.jallcom.2019.153096

22. Bisen S, Khan M, Mishra A (2020) Tailoring effect of large polaron hopping in the conduction mechanism of Ca-modified BaTiO3 system. Journal of Materials Science: Materials in Electronics 31:9212–9223. https://doi.org/10.1007/s10854-020-03452-1

23. Pritam A, Shrivastava V (2020) Deviations from Vegard's Law and Intense Raman Scattering in Low-Doped Bi2Mo1−xWxO6 (x = 0–10%) Ceramics. Phys Status Solidi B Basic Res 257:. https://doi.org/10.1002/pssb.201900450

24. Shahmoradi Y, Souri D (2019) Growth of silver nanoparticles within the tellurovanadate amorphous matrix: Optical band gap and band tailing properties, beside the Williamson-Hall estimation of crystallite size and lattice strain. Ceram Int 45:7857–7864. https://doi.org/10.1016/j.ceramint.2019.01.094

25. Nath D, Singh F, Das R (2020) X-ray diffraction analysis by Williamson-Hall, Halder-Wagner and size-strain plot methods of CdSe nanoparticles- a comparative study. Mater Chem Phys 239:. https://doi.org/10.1016/j.matchemphys.2019.122021

26. Aly KA, Khalil NM, Algamal Y, Saleem QMA (2017) Estimation of lattice strain for zirconia nano-particles based on Williamson- Hall analysis. Mater Chem Phys 193:182–188. https://doi.org/10.1016/j.matchemphys.2017.01.059

27. Harjo S, Tomota Y, Torii S, Kamiyama T (2002) Residual Thermal Phase Stresses in α-γ Fe-Cr-Ni Alloys Measured by a Neutron Diffraction Time-of-Flight Method

28. Sivakami R, Dhanuskodi S, Karvembu R (2016) Estimation of lattice strain in nanocrystalline RuO2 by Williamson-Hall and size-strain plot methods. Spectrochim Acta A Mol Biomol Spectrosc 152:43–50. https://doi.org/10.1016/j.saa.2015.07.008

29. Panda D, Hota SS, Choudhary RNP (2023) Investigation of structural, microstructural, dielectric, and electrical characteristics of a new lead-free compound: Ca3Bi2MoO9. Journal of Materials Science: Materials in Electronics 34:. https://doi.org/10.1007/s10854-023-11326-5

30. Pritam A, Shrivastava V (2020) Microwave derived porosity in tin-doped Sr1-xSnxBi1.95La0.05Nb2O9 nano materials for non-Debye conduction and photocatalytic activity. Physica B Condens Matter 593:. https://doi.org/10.1016/j.physb.2020.412320

31. Jena R, Chandrakanta K, Pal P, et al (2021) Dielectric relaxation and conduction mechanism in Aurivillius ceramic Bi5Ti3FeO15. International Journal of Minerals, Metallurgy and Materials 28:1063–1071. https://doi.org/10.1007/s12613-020-2091-3

32. Bhadauria PPS, Kolte J (2022) Impedance and AC conductivity analysis of La-substituted 0.67BiFeO3–0.33BaTiO3 solid solution. Appl Phys A Mater Sci Process 128:. https://doi.org/10.1007/s00339-022-05600-2

33. Verma M, Tanwar A, Haridas D, et al (2022) Effect of calcination temperature on structural, dielectric and piezoelectric properties of strontium bismuth niobate ceramics. Appl Phys A Mater Sci Process 128:. https://doi.org/10.1007/s00339-022-05954-7

34. Pritam A, Kumar S, Shrivastava V, et al (2024) Probing the effect of LaFeO3 on the structural, electrical, and dielectric properties of Sr0.8Sn0.2Bi2Nb2O9 processed through solid state route method. Mater Chem Phys 316:129089. https://doi.org/10.1016/j.matchemphys.2024.129089

35. Coondoo I, Jha AK, Agarwal SK (2007) Enhancement of dielectric characteristics in donor doped Aurivillius SrBi2Ta2O9 ferroelectric ceramics. J Eur Ceram Soc 27:253–260. https://doi.org/10.1016/j.jeurceramsoc.2006.04.167

36. Mitra S, Kulkarni AR, Prakash O Diffuse phase transition and electrical properties of lead-free piezoelectric (Li x Na 1-x)NbO 3 (0.04 ≤ x ≤ 0.20) ceramics near morphotropic phase boundary

37. Sharma VK, Nathawat R, Rathore SS (2022) Dielectric properties correlation with microstructure in ABi4Ti4O15 (A = Sr, Ba) bismuth layered ferroelectrics. Mater Adv 3:4890–4898. https://doi.org/10.1039/d2ma00333c

38. Shrivastava V, Pritam A, Joshi A (2018) Integrating third phase transition and CO/CO2 contamination in microwave tailored Bi2Mo1−xWxO6 nano materials. Journal of Materials Science: Materials in Electronics 29:17388–17396. https://doi.org/10.1007/s10854-018-9836-z

39. Shrivastava V (2016) Lattice strain driven dielectric insulation response of Sr1-xCaxBi2Nb2O9 ceramics. J Adv Dielectr 6:1650021-1-1650021–6. https://doi.org/10.1142/S2010135X16500211

40. Verma M, Tanwar A, Sreenivas K, Gupta V (2010) Dielectric and ferroelectric properties of SrBi2Nb 2O9 and SrBi1.9La0.1Nb 2O9 ceramics. In: Ferroelectrics. pp 233–239

41. Dhifallah N, Hehlen B, Khemakhem H (2022) Electrical conductivity and impedance spectroscopy studies of ceramic (Ba0.8Sr0.2)Ti0.95(Zn1/3Nb2/3)0.05O3 doped with Bi2O3. Solid State Commun 358:. https://doi.org/10.1016/j.ssc.2022.115003

42. SINGH R, Luthra V, Tandon RP (2016) Effect of Microwave Sintering on Electrical Properties of Sr-deficient and Bi-rich Strontium Bismuth Niobate (Sr0.8Bi2.2Nb2O9) Ferroelectric Ceramic. Journal of Modern Materials 1:35–45. https://doi.org/10.21467/jmm.1.1.35-45

43. Khan B, Singh MK, Yadav P, et al (2022) Optical properties, dielectric relaxor behavior, impedance and modulus spectroscopy of 0.8BiFeO3-0.2CaTiO3 composite. Mater Chem Phys 290:. https://doi.org/10.1016/j.matchemphys.2022.126642

44. El Heda I, Massoudi J, Dhahri R, et al (2023) Physical properties of substituted M0.5Fe2.5O4 ferrite spinels with M= (Mn and Zn). J Alloys Compd 931:. https://doi.org/10.1016/j.jallcom.2022.167479

45. Pritam A, Bhattacharya G, Sain S, et al (2024) Multiple relaxation mechanisms in SrBi2Nb2O9 ceramic tweaked by tin and samarium incorporation in assistance with single-step microwave sintering. Appl Phys A Mater Sci Process 130:. https://doi.org/10.1007/s00339-024-07482-y

46. Khatri P, Behera B, Srinivas V, Choudhary RNP (2008) Complex impedance spectroscopic properties of Ba3V 2O8 ceramics. Advances in Materials Science and Engineering 2008:. https://doi.org/10.1155/2008/746256